Theoretical Analysis of Modulation Response and Second-Order Harmonic Distortion in Vertical-Cavity Surface-Emitting Lasers

S. F. Yu, W. N. Wong, P. Shum, and E. Herbert Li, *Senior Member*

Abstract—**A rate-equation model is developed, with the consideration of size effects, to analyze the steady state and dynamic behavior of index-guided vertical-cavity surface-emitting lasers. The size dependence of spatial hole burning, cavity loss, as well as thermal resistance of device cavity are taken into account. Using this model, the influence of size effects on the amplitude modulation response and second-order harmonic distortion are studied. It is found that a laser with a small core radius exhibits better modulation response and less harmonic distortion than that of a large waveguide device, however, there is a tradeoff between the output power and modulation efficiency of the lasers.**

I. Introduction

VERTICAL-CAVITY surface-emitting lasers (VCSEL's) are promising for the applications in high-speed optical fiber communication systems due to its capability for single longitudinal mode operation, low threshold current, and narrow output beam profile. Furthermore, high relaxation oscillation frequency (ROF) is expected for VCSEL's due to its small cavity dimension. However, the modulation response of VCSEL's is limited by the combination of heat generation inside the high-resistance Bragg reflectors and parasitic capacitance due to interconnects on conducting substrates. In addition, differences in device structure also affected their high-speed modulation performance [1,2].

The steady-state properties of VCSEL's have been analyzed extensively and most of the works are concentrated on the improvement of quantum efficiency as well as reduction of threshold current. Models including temperature effects, carrier spatial hole burning, as well as surface scattering and diffraction losses have been developed to predict the performance of lasers with different dimensions and structures [3], [4]. However, the relatively important behavior of VCSEL's, the dynamic response under direct modulation, has not been considered in their investigation. In this paper, we analyze the small-signal response of index-guided VCSEL's with size dependent of spatial hole burning, cavity loss, as well as thermal resistance of laser cavity taken into account. The spatial hole burning effects are approximated by a perturbation approach [5] in our model. Furthermore, the thermal rate equation is simplified to a nonlinear differential equation by replacing the divergence of the heat flux with an equivalent thermal resistor [6]. The size dependence of thermal resistance and cavity loss can be determined by matching with the experimental data (i.e., threshold current and external quantum efficiency). Using this model, the modulation responses of VCSEL's under the influence of size effects as well as other inherent nonlinearities are studied. In Section II, a rate-equation model of VCSEL's is developed with the consideration of self-heating, spatial hole burning, and carrier transport. In Section III, this model is applied to study the steady state and dynamic behavior of VCSEL's. We can also verify that the fitted parameters give a consistent explanation for the size dependence of threshold current. In addition, the amplitude modulation (AM) response and second-order harmonic distortion (SHD) of VCSEL's are also analyzed. Discussions on the dynamic performance of VCSEL's are given in Section VI.

Manuscript received January 15, 1996; revised June 10, 1996. This work was supported by CRCG Grant 337/062/0035.

The authors are with the Department of Electrical and Electronic Engineering, University of Hong Kong, Pokfulam Road, Hong Kong.

Publisher Item Identifier S 0018-9197(96)08666-6.

II. Laser Model

A. General Rate Equations of VCSEL's

A simple rate-equation model with the inclusion of inherent nonlinearities such as self-heating, spatial hole burning, and carrier transport to calculate the influence of device dimension on the modulation response of VCSEL's are given as

$$\frac{\partial S}{\partial t} = \nu_g(\Gamma_z G - \alpha_t)S + \beta B_{sp} N^2 \tag{1}$$

$$\frac{\partial N}{\partial t} = \frac{M}{\tau_{12}} - \frac{N}{\tau_C} - \frac{N}{\tau_{21}} - \nu_g \Gamma_z g(N)|\Psi|^2 S + D\frac{1}{r}\frac{\partial}{\partial r}\left(r\frac{\partial N}{\partial r}\right) \tag{2}$$

$$\frac{\partial M}{\partial t} = \frac{J}{eL_z N_w} - \frac{M}{\tau_C} - \frac{M}{\tau_{12}} + \frac{N}{\tau_{21}} \tag{3}$$

$$\rho_m C_p \frac{\partial T}{\partial t} = \nabla \cdot (\kappa \nabla T) + H_{cv} \tag{4}$$

where S is the photon density, N is the carrier concentration inside the active layer, M is the carrier concentration confined inside the spacer layers, and T is the effective temperature of laser cavity. In the photon rate equation, ν_g is the group velocity, Γ_z is the longitudinal optical confinement factor, α_t is the equivalent modal loss, β is the spontaneous emission factor, and B_{sp} is the bimolecular carrier recombination coefficient. In the carrier rate equations, τ_C is the carrier lifetime and D is the ambipolar diffusion coefficient. The influence of carrier transport is described by τ_{12}, the carrier transport time in the

spacer layers, and τ_{21}, the thermionic capture/emission time. The total thickness of the active layer is the multiplication of quantum well thickness, L_z, with the number of quantum wells, N_w. J and e given in (3) are the injection current density and electron charge, respectively. In the thermal rate equation, ρ_m is the mass density, C_p is the heat capacity, and κ is the thermal diffusion coefficient of semiconductor material. H_{cv} is defined as the average thermal power density generated inside the laser cavity.

The optical field distribution, Ψ, is assumed cylindrically symmetric and satisfies the unperturbed wave equation

$$\frac{\partial^2\Psi(r)}{\partial r^2}+\frac{1}{r}\frac{\partial\Psi(r)}{\partial r}+(\varepsilon_o k_o^2-\beta^2)\Psi(r)=0 \tag{5}$$

where $k_o=(2\pi/\lambda_o)$ is the wavevector, ε_o is the background dielectric constant, and β is the propagation constant to be determined.

For quantum well material, the optical gain, g, given in (2) can be written as [7]

$$g(N)=a_N ln\,(N/N_t) \tag{6}$$

where a_N is a fitted parameter and N_t is the carrier concentration at transparency. The parameters a_N and N_t are also varied with temperature and their dependence can be approximated by the empirical formulas given in [3] and [8]. G, given in (1), can be expressed as

$$G=\int_0^w g(N)|\Psi(r)|^2 r\,dr\Big/\int_0^\infty |\Psi(r)|^2 r\,dr \tag{7}$$

and w is the radius of core. The output power $P_{h\nu}$ of the device is given by

$$P_{h\nu}=\tfrac{1}{2}\nu_g(1-|r_{\text{eff}}|^2)\pi w^2\Gamma_z S \tag{8}$$

where h is the Planck's constant, $|r_{\text{eff}}|$ is the effective reflectivity of the Bragg reflector and ν is the operation frequency of the laser.

B. Approximation on the Spatial Hole Burning and Divergence of Thermal Flux

In (1)–(3), M and N are nonuniformly distributed along the lateral direction, r. However, it is noted that for our previous analysis of VCSEL's [8], the lateral distribution of carrier concentration along the spacer layers is quite uniform. Furthermore, the spatial hole burning inside the active layer is less than 10% of its peak magnitude. Therefore, it is reasonable to assume M is uniform along the lateral direction and the nonuniform distribution of N is approximated by a perturbation approach [5]

$$N=N_p-N_sJ_0(ar) \tag{9}$$

where N_p is the average carrier concentration along the lateral direction and N_s is the perturbation of carrier concentration arisen from $\Psi(r)$ (see Fig. 1). $J_o(ar)$ is the Bessel function of first kind of order 0 and the constant a satisfies $J_1(aw)=0$. In (9), only the fundamental lateral mode is considered in the analysis. We have assumed that the carrier concentration is

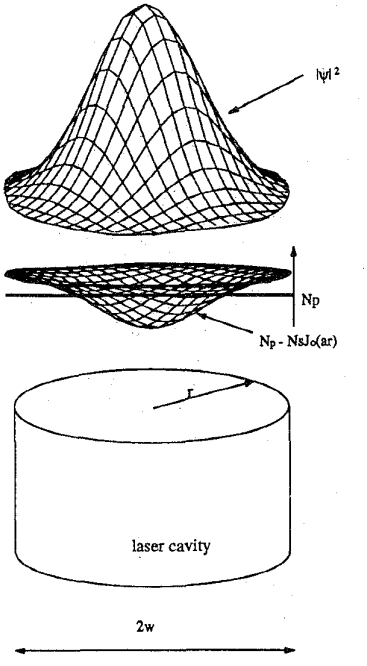

Fig. 1. Distribution of carrier concentration and optical field intensity inside the cylindrical laser cavity.

well confined inside the core region. For N_s is smaller than N_p, the optical gain can also be written as

$$\begin{aligned} g(N)&=a_N\ln(N/N_t)\\ &\approx a_N[\ln(N_p/N_t)-(N_s/N_p)J_0(ar)]. \end{aligned} \tag{10}$$

Substituting (9) and (10) into (1)–(3) and integrating along the lateral direction, we get

$$\begin{aligned} \frac{\partial S}{\partial t}&=\nu_g(a_N\Gamma_z[\Gamma_r\ln(N_p/N_t)-(N_s/N_p)\xi_r]-\alpha_t)S\\ &\quad+\beta B_{sp}N_p^2, \end{aligned} \tag{11}$$

$$\begin{aligned} \frac{\partial N_p}{\partial t}&=\frac{M}{\tau_{12}}-\frac{N_p}{\tau'_{21}}-D\chi_1N_s-\nu_g a_N\\ &\quad\cdot\Gamma_z[\Gamma_1\ln(N_p/N_t)-(N_s/N_p)\xi_1]S, \end{aligned} \tag{12}$$

$$\begin{aligned} \frac{\partial N_s}{\partial t}&=\nu_g a_N\Gamma_z[\Gamma_2\ln(N_p/N_t)-(N_s/N_p)\xi_2]S\\ &\quad+[D\chi_2-1/\tau'_{21}]N_s, \end{aligned} \tag{13}$$

$$\frac{\partial M}{\partial t}=\frac{J}{eL_zN_w}-\frac{M}{\tau'_{12}}+\frac{N_p}{\tau_{21}} \tag{14}$$

where $1/\tau'_{21}=1/\tau_c+1/\tau_{21}, 1/\tau'_{12}=1/\tau_c+1/\tau_{12}$. The size effects related to converting the carriers into photon have been considered in (12)–(14) through the size-dependent parameters (i.e., $\Gamma_r,\xi_r,\Gamma_1,\xi_1,\Gamma_2,\xi_2,\chi_1$, and χ_2) and their expression can be found in Appendix A.

The temperature dependence of threshold current density J_{th} (300 °K) is described by the Arrhenius-type relation [9]

$$J_{\text{th}}(T)=J_o\exp\left(\frac{T-300}{T_o}\right) \tag{15}$$

where J_o is the threshold current at 300 °K and T_o is the characteristic temperature. J_o can be expressed as J_o =

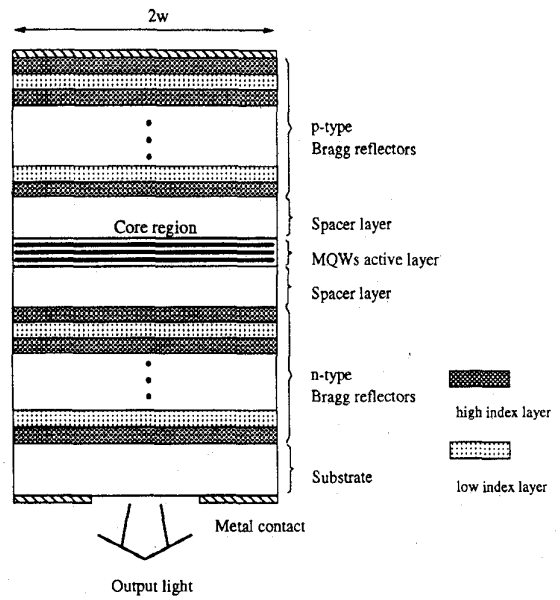

Fig. 2. Schematic of an index-guided VCSEL.

TABLE I
PARAMETER USED IN THE MODEL

Parameter	Symbol	Value
lasing wavelength	λ_o	0.98μm
group velocity	v_g	0.83×10^{10}cm/s
longitudinal optical confinement factor	Γ_z	0.065
bimolecular carrier recombination coefficient	B_{sp}	1×10^{-10}cm^{3}s^{-1}
spontaneous emission factor	β	1×10^{-4}
carrier lifetime in active layer	τ_C	3×10^{-9} s
carrier transport time in the spacer layers	τ_{12}	10–20ps
thermionic capture/emission time	τ_{21}	200ps
diffusion rate coefficient	D	5–20s^{-1}cm^2
thickness of quantum well	L_z	80Å
number of quantum well	N_w	3
mass density	ρ_m	5.36gcm^{-3}
specific heat	C_p	0.35Jg^{-1}C^{-1}
thermal conductivity	κ	0.45–0.55Wcm^{-1}C^{-1}
effective reflectivity of Bragg reflector	$\lvert r_{eff}\rvert$	0.9995
characteristic temperature	T_o	110°K

$eL_zN_wN_{\rm th}/\tau_c$ where $N_{\rm th}$ is the threshold carrier concentration at 300 °K.

Furthermore, using the technique in [6] of replacing the divergence of heat flux with an equivalent thermal resistor $R_{\rm th}$ (cm^{-1}) representing both the active layer and Bragg reflectors, we can rewrite (4) as the nonlinear differential equation

$$C_{\rm th}\frac{\partial T}{\partial t} = (P_{IV} - P_{h\nu}) - \kappa\frac{\Delta T}{R_{\rm th}} \tag{16}$$

where $C_{\rm th}$ $(= \rho_m C_p \pi w^2 N_w L_z)$ is defined as the thermal capacitance. P_{IV} is the total input electrical power and can be expressed as

$$P_{IV} = \tfrac{1}{2}\int_0^{2\pi}\int_0^{w} V_F(N)J(r)r\,dr\,d\theta. \tag{17}$$

V_F given in (17) is the voltage across the active layer and is given by [10]

$$V_F = \frac{1}{q}[E_g + k_BT\cdot\ln\{(\exp(N/N_c)-1)\cdot(\exp(N/N_v)-1)\}] \tag{18}$$

where E_g $(= 1.519\text{–}5.408\times10^{-4}\times T^2/(T+204))$ is the effective energy gap of the quantum well's active layer and k_B is the Boltzmann constant. N_c and N_v are the effective conduction and valence edge density of states, respectively, and can be expressed as

$$N_{c/v} = m^*_{e/h}k_BT/\pi\hbar^2L_z \tag{19}$$

where $\hbar = h/2\pi$, and $m^*_{e/h}$ is the effective mass of electron/holes.

In (11) and (16), we have not specified the size dependence of α_t and $R_{\rm th}$. It is expected that the reduction of w causes the increase of $R_{\rm th}$. In addition, due to the increase of surface scattering and diffraction losses, α_t is also increased with the reduction of w. These phenomena of VCSEL's can be evaluated in detail by using the thermal equation [11] as well as the scattering and diffraction model of VCSEL's [12], however, this is not the scope of this paper. An alternative approach used in this paper is to fit these parameters with the experimental data given (i.e., the threshold current and the external quantum efficiency obtained from the light/current curves). This approach gives a satisfactory explanation of the physical phenomena of VCSEL's provided that α_t and $R_{\rm th}$ demonstrate an inverse relation with the device size (i.e., the reduction of w causes the increase of α_t and $R_{\rm th}$); otherwise this model fails to produce self-consistent results.

III. NUMERICAL RESULTS

The schematic of an index-guided VCSEL used in our analysis is shown in Fig. 2. The device structure is similar to that given in [2] and [3] except the p- and n-type distributed Bragg reflectors have equal core diameter in order to simplify our calculation. The waveguide (core) region is surrounded by air and its effective refractive index is equal to 3.30. The background temperature is set to 300 °K. In addition, the injection current is assumed uniformly distributed along the lateral direction. Furthermore, only the fundamental lateral mode is considered in our analysis as we have assumed in the derivation of (11)–(16). The steady-state characteristics of VCSEL's can be calculated by using the Newton Raphson method. In addition, using (11)–(16), the AM and SHD of VCSEL's can also be determined by the small-signal analysis, and the derivation procedures are similar to those in [13]. The laser and size-dependent (i.e., $\Gamma_r, \xi_r, \Gamma_1, \xi_1, \Gamma_2, \xi_2, \chi_1$ and χ_2) parameters used in the model are shown in Tables I and II.

A. Influence of Waveguide Dimension on the Static and Dynamic Behavior of VCSEL's

Fig. 3(a) shows the measured light/current curves (dotted lines) of VCSEL's obtained from [2]. It is shown that the output power is saturated at high injection current and the peak power is reduced with the core radius. There are several effects

TABLE II
PARAMETERS DEFINING THE TRANSVERSE STRUCTURE OF THE VCSEL'S

parameters\w	2.5μm	3.5μm	5.0μm	7.5μm
Γ_r	0.9999	0.9999	0.9999	0.9999
ξ_r	0.4148	0.4165	0.4182	0.4194
Γ_1	0.2744	0.2731	0.2720	0.2704
ξ_1	0.1138	0.1138	0.1137	0.1137
Γ_2	0.7014	0.7013	0.7012	0.7011
ξ_2	0.5287	0.5279	0.5271	0.5261
χ_1	-8.9085×10^{-4}	-4.9350×10^{-4}	-2.3081×10^{-4}	0.6285×10^{-4}
χ_2	-2.1426×10^{8}	-0.9167×10^{8}	-0.5684×10^{8}	-0.500×10^{8}

TABLE III
SIZE DEPENDENCE OF OPTICAL LOSS AND THERMAL RESISTANCE OF VCSEL'S

core radius w (μm)	optical loss α_t (cm^{-1})	Thermal Resistance R_{th} (cm^{-1})
2.5	72	4500
3.5	59	2600
5	46	1660
7.5	38	990

responsible for the reduction of output power as the core radius is reduced. They are: 1) the thermal resistance of VCSEL's which is inversely proportional to the core radius (i.e., small devices suffer high thermal dissipation); 2) the size dependence of cavity loss due to the surface scattering and diffraction losses; and 3) the increase in threshold current density with the junction temperature. In fact, these phenomena have been introduced into the rate-equation model through: 1) the thermal resistance $R_{\rm th}$ defined in (16); 2) the equivalent model loss defined in (1); and 3) the threshold current density which is approximated by the Arrhenius-type relation [see (15)]. Using the measured light/current curves given in Fig. 3(a), the parameters α_t and $R_{\rm th}$ can be evaluated, and their magnitude are shown in Table III. The corresponding calculated light/current curves (solid lines) are also shown in the figure for comparison. In the calculation, it is assumed that $D = 5\ \mathrm{s}^{-1}\ \mathrm{cm}^2, \tau_{12} = 10$ ps, and $\kappa = 0.45\ \mathrm{Wcm}^{-1}\mathrm{C}^{-1}$.

In Table III, both α_t and $R_{\rm th}$ exhibit an inverse relation with w which indicated that the rate-equation model gives a satisfactory explanation on the physical phenomena of VCSEL's. Furthermore, the variation of threshold current $I_{\rm th}$ with the device size can also be explained by the following equations:

$$J_{\rm th} \approx eL_zN_wN_{\rm th}/\tau_C \tag{20}$$

$$G_{\rm th} = \alpha_t = a_N \ln\left(N_{\rm th}/N_t\right) \tag{21}$$

where $J_{\rm th}$ is the threshold current density, $N_{\rm th}$ is the threshold carrier concentration, and $G_{\rm th}$ is the threshold gain. Obviously, the increase in device size implies the decrease in $N_{\rm th}$ and $J_{\rm th}$. For an air-post VCSEL, $I_{\rm th}$ is equal to $AJ_{\rm th}$ where $A\ (=\pi w^2)$ is the junction area. Therefore, the decrease of $J_{\rm th}$ does not imply the decrease of $I_{\rm th}$, as the reduction of $J_{\rm th}$ is compensated by the increase of A such that $I_{\rm th}$ can be maintained nearly constant for some range of device radius, w (i.e., 2.5 to 5 μm). However, $I_{\rm th}$ increases for $w > 5$ μm because the rate of change of α_t is less than that of A. This phenomenon of VCSEL's has been observed from the experimental data and can be explained by our simple model.

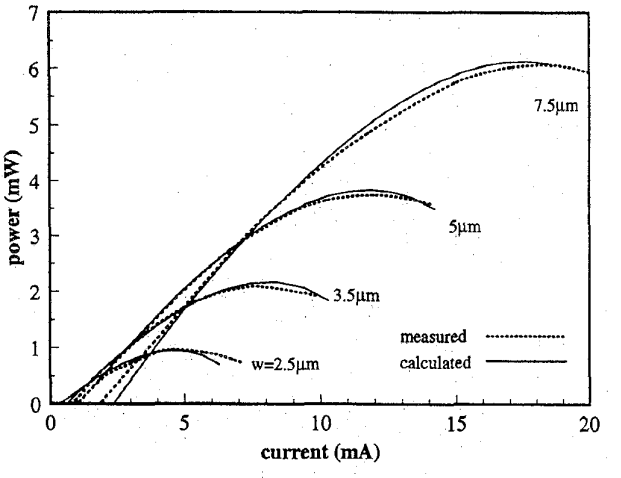

(a)

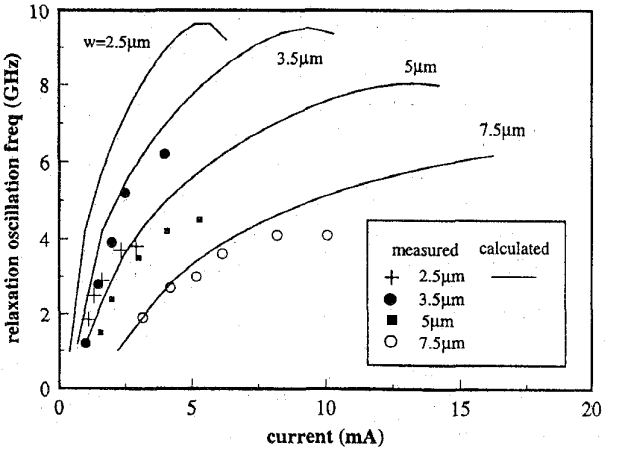

(b)

Fig. 3. Comparison of measured and calculated (a) light/current characteristics and (b) ROF of VCSEL's with core radius equal to 2.5, 3.5, 5.0, and 7.5 μm. It is assumed that $D = 5\ \mathrm{s}^{-1}\mathrm{cm}^2, \tau_{12} = 10$ ps and $\kappa = 0.45\ \mathrm{Wcm}^{-1}\ \mathrm{C}^{-1}$ in the calculation.

Therefore the relation between threshold current and device size can also be predicted by the model.

Fig. 3(b) compares the calculated and measured ROF [2] of VCSEL's. It must be noted that the ROF is calculated without optimizing the fitted parameters α_t and $R_{\rm th}$ [i.e., α_t and $R_{\rm th}$ are only evaluated from the light/current curves given in Fig. 3(a)]. In general, the measured results show that small devices exhibit high modulation efficiency as well as saturation level of ROF (i.e., peak ROF). However, the modulation efficiency of the smallest laser ($w = 2.5$ μm) is not the highest (device of $w = 3.5$ has the highest modulation efficiency). This is attributed to the high optical loss of small VCSEL's that drives the threshold gain toward the saturation levels of quantum wells which reduces the differential gain and hence the modulation efficiency [2]. This phenomenon has not been taken into account in the model, however, for devices with $w \geq 3.5$ μm, the agreement between the theoretical prediction and measured results [as shown in Fig. 3(b)] is satisfied considering the simplicity of the model. Therefore,

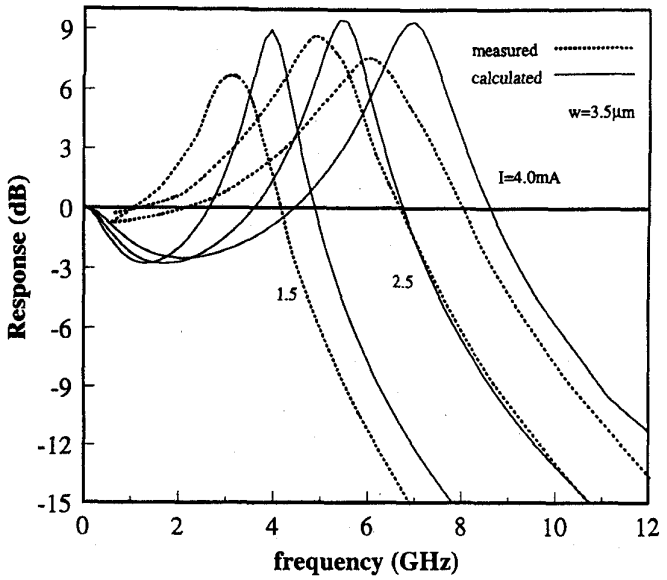

Fig. 4. Comparison of measured and calculated amplitude modulation response of VCSEL with a core radius of 3.5 μm.

the gain saturation effects due to the high optical loss have less influence on large area devices ($w \geq 3.5$ μm) and is ignored in the following calculation. The AM response of a 3.5-μm radius VCSEL for various bias currents is also given in Fig. 4.

The analytical expression of ROF, ω_n, is given by

$$\omega_n^2 \approx \Gamma_r \Gamma_1 (\nu_g a_N \Gamma_z)^2 \ln (N_{po}/N_t)(S_0/N_{p0})^2 \qquad (22)$$

where the subscript 0 stands for the steady state. In (22), the influence of D and τ_{12} are ignored and the detailed derivation of ω_n can be found in Appendix B. In (22), ω_n is directly proportional to S_0 such that the magnitude of ω_n is also saturated. The modulation efficiency, $\partial\omega_n/\partial I$, can also be deduced from (22) for injection current, I, less than 5 mA (i.e., light/current gives a linear relation):

$$\partial\omega_n/\partial I \approx \gamma\nu_g(1/w^2)(a_N/N_{p0})\sqrt{\Gamma_r\Gamma_1 \ln (N_{p0}/N_t)} \qquad (23)$$

where γ $(= 2\eta/\nu_g h\nu(1 - |r_{\text{eff}}|^2)\pi)$ is a constant and η is the slope of the light/current curves. As we can see, $\partial\omega_n/\partial I$ is inversely proportional to waveguide area such that small devices have better modulation efficiency. In addition, the effective threshold current is increased with the junction temperature, but the differential gain, a_N/N_{p0} is reduced. It must be noted that heat generation is more rapid in small devices such that fast saturation of ω_n with injection current is observed in Fig. 3(b).

Fig. 5 shows the AM response of VCSEL's with core radii varying between 3.5 and 7.5 μm. The devices are biased such that the output power is equal to 1 mW. As we can see, a small device has better modulation response than large-area lasers. The corresponding SHD of VCSEL's is also shown in Fig. 6. VCSEL with small core radius exhibits less SHD. Two resonance peaks appear and the second peak is caused by resonance in the AM response and will not occur if a constant optical modulation depth is considered [13].

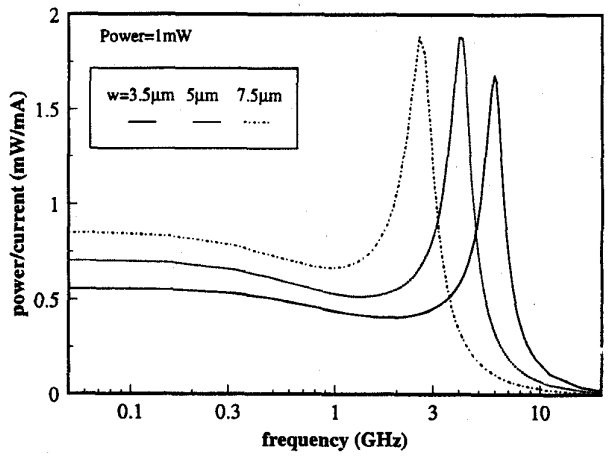

Fig. 5. Amplitude modulation response of VCSEL's with core radii equal to 3.5, 5.0, and 7.5 μm. The steady-state output power of all VCSEL's is 1 mW.

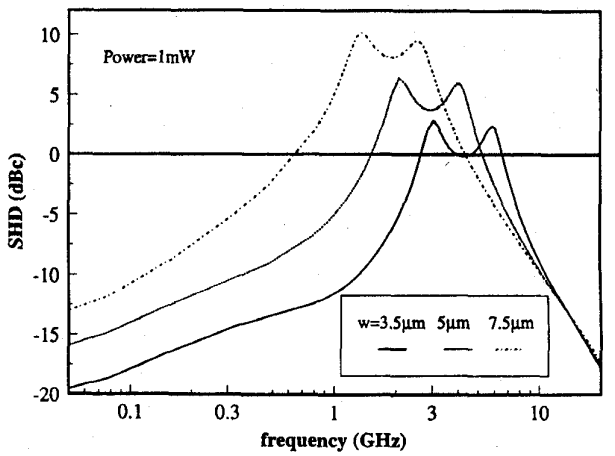

Fig. 6. Second harmonic distortion of VCSEL's with core radii equal to 3.5, 5.0, and 7.5 μm. The steady-state output power of all VCSEL's is 1 mW.

B. Influence of Spatial Hole Burning, Carrier Transport, and Thermal Effects on the Static and Dynamic Behavior of VCSEL's

The influence of spatial hole burning and carrier transport on the static and dynamic response of VCSEL's is studied. These nonlinearities are examined by changing the diffusion rate D from 5 to 10 $\text{cm}^2\,\text{s}^{-1}$ and the carrier transport time τ_{12} from 10 to 20 ps for devices with core radii equal to 3.5 and 7.5 μm. Fig. 7 shows the corresponding light/current curves and ROF of VCSEL's. D and τ_{12} have relatively less influence on the static and dynamic behavior of VCSEL's. The influence of spatial hole burning and carrier transport on the AM response and SHD of VCSEL's are also shown in Figs. 8 and 9 for devices of $w = 3.5$ and 7.5 μm. The lasers are biased such that the output power is equal to 1 mW. The overshoot of AM response is affected by both D and τ_{12}. On the other hand, these inherent nonlinearities have less influence on the SHD of VCSEL's.

As shown in the above paragraph, the peak output power of VCSEL's is less dependent on the spatial hole burning and carrier transport. In order to improve the maximum

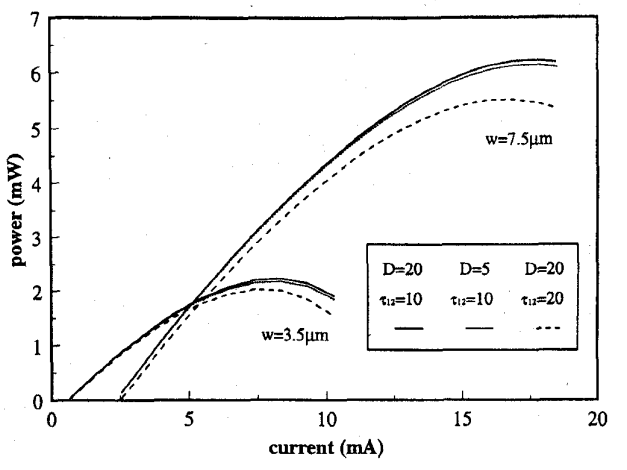

(a)

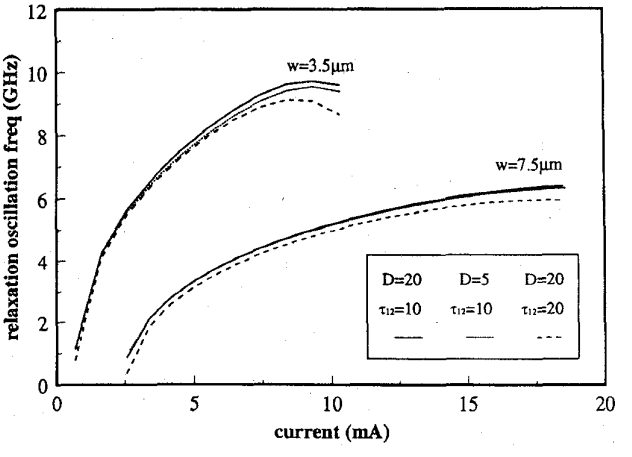

(b)

Fig. 7. Calculated (a) light/current characteristics and (b) ROF of VCSEL's under the influence of D and τ_{12}. Solid lines: $D = 20$ s^{-1} cm^2 and $\tau_{12} = 10$ ps; dotted lines: $D = 5$ s^{-1} cm^2 and $\tau_{12} = 10$ ps; and dashed lines: $D = 20$ s^{-1} cm^2 and $\tau_{12} = 20$ ps.

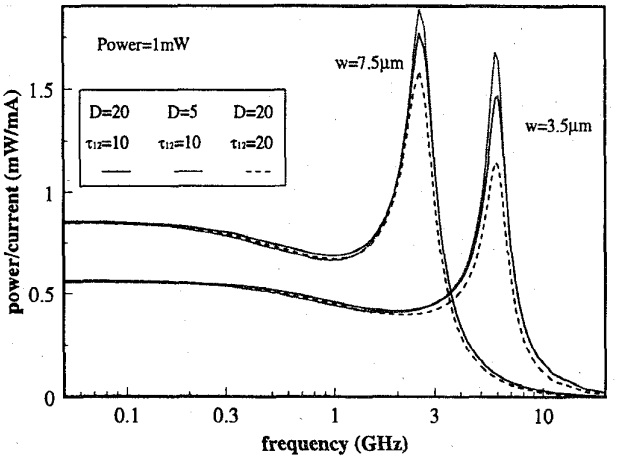

Fig. 8. Amplitude modulation response of VCSEL's with core radii of 3.5 and 7.5 μm under the influence of D and τ_{12}. The steady-state output power of lasers is 1 mW. Solid lines: $D = 20$ s^{-1} cm^2 and $\tau_{12} = 10$ ps; dotted lines: $D = 5$ s^{-1} cm^2 and $\tau_{12} = 10$ ps; and dashed lines: $D = 20$ s^{-1} cm^2 and $\tau_{12} = 20$ ps.

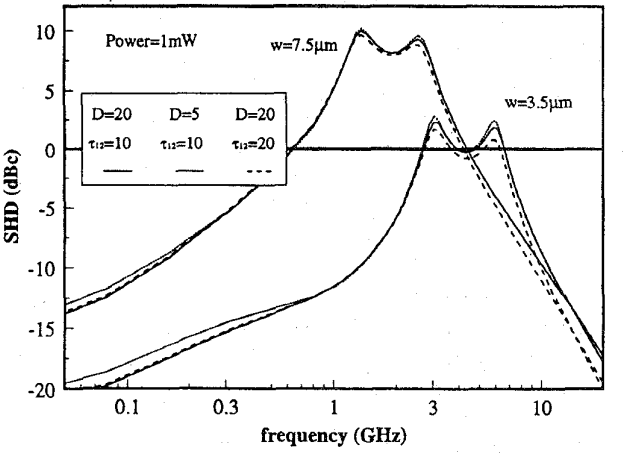

Fig. 9. Second harmonic distortion of VCSEL's with core radii of 3.5 and 7.5 μm under the influence of D and τ_{12}. The steady-state output power of lasers is 1 mW. Solid lines: $D = 20$ s^{-1} cm^2 and $\tau_{12} = 10$ ps; dotted lines: $D = 5$ s^{-1} cm^2 and $\tau_{12} = 10$ ps; and dashed lines: $D = 20$ s^{-1} cm^2 and $\tau_{12} = 20$ ps.

output power and modulation efficiency of VCSEL's, the thermal resistance of the laser cavity should be reduced to avoid excess self-heating. To verify the above statement, we analyze the influence of thermal conductivity κ on the static and dynamic behavior of VCSEL's. Fig. 10(a) shows the light/current curves of devices with radii equal to 3.5 and 7.5 μm. The thermal conductivity of VCSEL's κ is varied between 0.45 and 0.55 Wcm^{-1} C^{-1}. D and τ_{12} are set to 20 cm^2 s^1 and 10 ps, respectively. As we can see, the maximum output power is enhanced by several milliwatts. The corresponding ROF is also shown in Fig. 10(b). It is shown that the ROF is enhanced for both devices but small-area devices have better improvement. The AM response and SHD under the influence of κ are also shown in Figs. 11 and 12, respectively. It is assumed that the output power of devices is equal to 1 mW. As we can see, κ has no negative effects on both AM response and SHD of VCSEL's. From our theoretical analysis given above, we can conclude that the thermal effects determined the ROF of lasers, however, the AM and SHD are less dependent on this factor.

IV. Discussion and Conclusion

The dependence of device size on the modulation response of VCSEL's can be explained by (22) and (23). In (22), ROF is directly proportional to the photon density S_0 such that ROF is saturated with injection current. It is noted that a small laser has large thermal resistance and the ROF is saturated faster with injection current due to the temperature dependence of a_N and N_t. In addition, the modulation efficiency is inversely proportional to the waveguide area as shown in (23) such that a small device ($w = 3.5$ μm) exhibits better modulation efficiency. For devices smaller than 3.5 μm in radius, gain saturation effects due to high optical loss should be taken into consideration in the model. The spatial hole burning has less influence on the ROF of VCSEL's and is clearly explained by (B11) of Appendix B. This is because spatial hole burning is determined by the parameter ε_s but this parameter is only

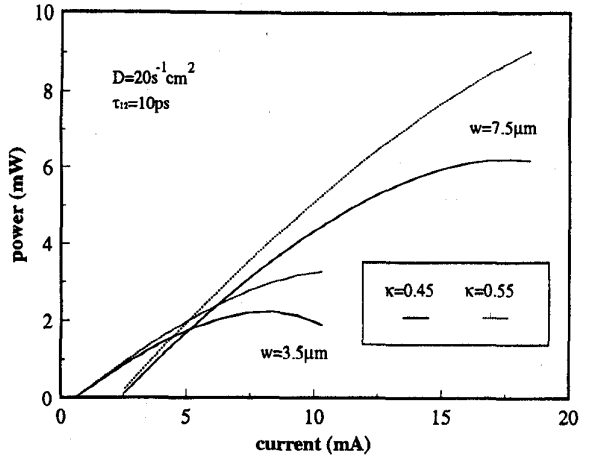

(a)

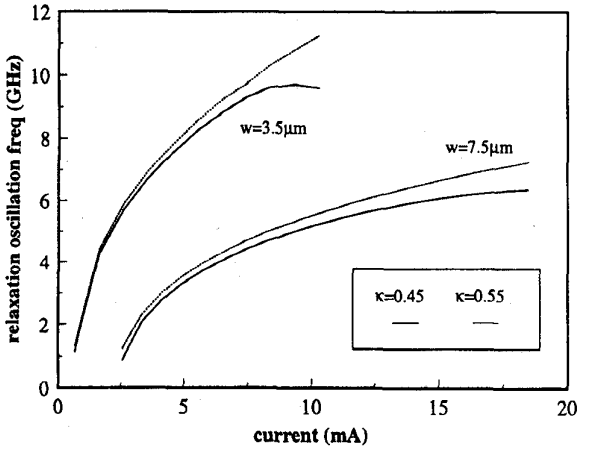

(b)

Fig. 10. Calculated (a) light/current characteristics and (b) relaxation oscillation frequency of VCSEL's with core radii of 3.5 and 7.5 μm under the influence of κ. Solid lines: $\kappa = 0.45$ Wcm^{-1} C^{-1}; and dotted lines: $\kappa = 0.55$ Wcm^{-1} C^{-1}.

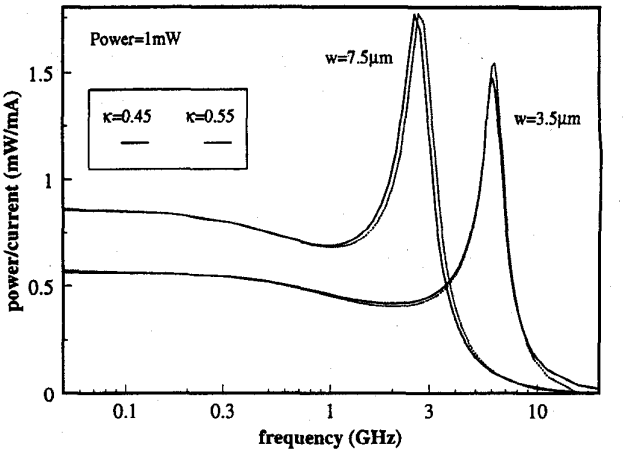

Fig. 11. Amplitude modulation response of VCSEL's with core radii of 3.5 and 7.5 μm under the influence of κ. The steady-state output power of the lasers is 1 mW. Solid lines: $\kappa = 0.45$ Wcm^{-1} C^{-1}; and dotted lines: $\kappa = 0.55$ Wcm^{-1} C^{-1}.

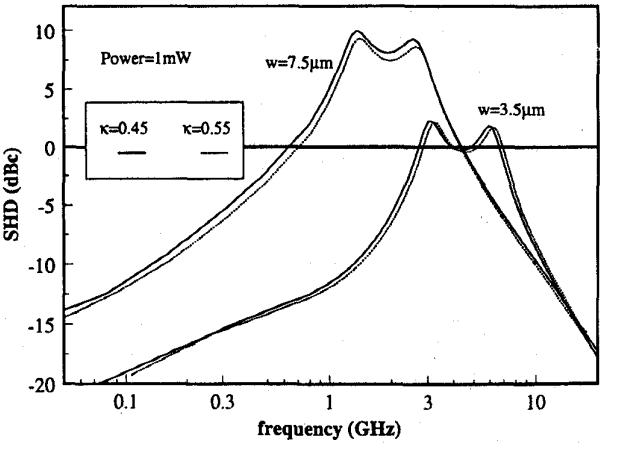

Fig. 12. Second harmonic distortion of VCSEL's with core radius of 3.5 and 7.5 μm under the influence of κ. The steady state output power of lasers is 1 mW. Solid lines: $\kappa = 0.45$ Wcm^{-1} C^{-1}; and dotted lines: $\kappa = 0.55$ Wcm^{-1} C^{-1}.

significant at high S_0. This conclusion, however, is different from [8] as the optical intensity and carrier concentration are well confined inside the air-post cavity. In (B10), the carrier transport effects may have crucial effects on the ROF as we have discussed in Appendix B. In order to maximize the ROF, it is desired to have large magnitude of τ_{21} but small τ_{12} to enhance the modulation bandwidth of the VCSEL's.

In conclusion, a rate-equation model for index-guided VCSEL's, including thermal effects, spatial hole burning, and carrier transport, has been developed. The purpose of this paper is to understand the influence of size effects on the modulation response of VCSEL's. Although this laser model is simple, it is able to explain the dependence of threshold current as well as the thermal resistance and cavity loss on the device size. It is shown that peak output power is limited by small waveguide area, however, high modulation efficiency is obtained. In addition, a small device exhibits better AM response and less harmonic distortion. We have also shown the importance of thermal effects on the modulation response of VCSEL's. It is noted that thermal effects dominate over other inherent nonlinearities on the influence of the dynamic behavior of VCSEL's. Slight increases in the thermal conductivity of the device enhances the saturated ROF by more than several gigahertz. From our analysis given above, we noted that reduction of heat generation inside the laser cavity is an alternative way to improve the dynamic behavior of small waveguide VCSEL's.

APPENDIX A

The expression of $\Gamma_r, \xi_r, \Gamma_1, \xi_1, \Gamma_2, \xi_2, \chi_1$ and χ_2 are given by

$$\Gamma_r = \int_0^w r|\Psi|^2\,dr \Big/ \int_0^\infty |\Psi(r)|^2 r\,dr \tag{A1}$$

$$\xi_r = \int_0^w rJ_0(ar)|\Psi|^2(r)\,dr \Big/ \int_0^\infty |\Psi(r)|^2 r\,dr \tag{A2}$$

$$\Gamma_1 = \frac{2}{w^2}\int_0^w r|\Psi|^2\,dr \tag{A3}$$

$$\xi_1 = \frac{2}{w^2}\int_0^w |\Psi|^2 J_0(ar) r\,dr \tag{A4}$$

$$\Gamma_2 = \frac{2}{w^2}\frac{1}{J_0^2(aw)}\int_0^w r J_0(ar)|\Psi|^2\,dr \tag{A5}$$

$$\xi_2 = \frac{2}{w^2}\frac{1}{J_0^2(aw)}\int_0^w r J_0^2(ar)|\Psi|^2\,dr \tag{A6}$$

$$\chi_1 = \frac{2}{w^2}\int_0^w \left(r\frac{\partial^2 J_0(ar)}{\partial r^2} + \frac{\partial J_0(ar)}{\partial r}\right)dr \tag{A7}$$

$$\chi_2 = \frac{2}{w^2}\frac{1}{J_0^2(aw)}\int_0^w J_0(ar)\left(r\frac{\partial^2 J_0(ar)}{\partial r^2} + \frac{\partial J_0(ar)}{\partial r}\right)dr. \tag{A8}$$

APPENDIX B

The number of rate equations given in Section II-B can be reduced by two using the quasi-static steady approximation on N_s and T to simplify the derivation of ROF. This can be done by setting the time derivative of (13) to zero for the reason of $(1 - D\chi_2\tau_{21}')/\tau_{21}'$ in (13) which has a value in the order of 100 ps and is short compared to the period of practical small-signal modulation waveforms [5]. Thus,

$$N_s = \frac{\varepsilon\Gamma_2 \ln(N_p/N_t)S}{1 + \varepsilon\xi_2(S/N_p)} \tag{B1}$$

where $\varepsilon = \nu_g a_N \Gamma_z \tau_{21}'/(1 - D\chi_2\tau_{21}')$. In addition, for devices with short cavity length and small surface area, the $R_{\rm th}C_{\rm th}/\kappa$ time constant is also in the order of 100 ps such that we can ignore the time derivative term in (16). Now, the corresponding rate equations are given by

$$\frac{\partial S}{\partial t} = \nu_g(a_n\Gamma_z\Gamma_r \ln(N_p/N_t)(1 - \varepsilon_s S/N_p) - \alpha_t) + \beta B_{sp}N_p^2 \tag{B2}$$

$$\frac{\partial N_p}{\partial t} = \frac{M}{\tau_{12}} - \frac{N_p}{\tau_{21}'} - \nu_g a_N \Gamma_z\Gamma_p \ln(N_p/N_t) \cdot (1 - \varepsilon_p S/N_p)S \tag{B3}$$

$$\frac{\partial M}{\partial t} = \frac{J}{eL_z N_w} - \frac{M}{\tau_{12}'} + \frac{N_p}{\tau_{21}} \tag{B4}$$

where $\varepsilon_s = \varepsilon(\Gamma_2\xi_r/\Gamma_r + \xi_2), \Gamma_p = \Gamma_1 + D\chi_1\tau_{21}\Gamma_2$ and $\varepsilon_p = \varepsilon((\Gamma_2\xi_r - \Gamma_1\xi_2)/\Gamma_p + \xi_2)$. The auxiliary thermal equation is given by $\Delta T = R_{\rm th}(P_{IV} - P_{h\nu})/\kappa$.

The relaxation oscillation of the laser can be derived from (B2)–(B4) by applying a small perturbation to J, S, N_p, and M from the steady state [13], and the corresponding characteristic polynomial of the laser is given by

$$\frac{1}{\tau_{12}\tau_{21}}\left(\frac{1}{T_{11}} + j\Omega\right) - \frac{1}{T_{12}T_{21}}\left(\frac{1}{\tau_{12}'} + j\Omega\right) - \left(\frac{1}{T_{11} + j\Omega}\right)\left(\frac{1}{T_{22}} + j\Omega\right)\left(\frac{1}{\tau_{12}'} + j\Omega\right) = 0 \tag{B5}$$

where Ω is the modulation frequency of the laser, and the expression of T_{11}, T_{12}, T_{21}, and T_{22} are shown below:

$$1/T_{11} = \nu_g a_N \Gamma_r\Gamma_z\varepsilon_s \ln(N_{p0}/N_t)S_0/N_{p0} \tag{B6}$$

$$1/T_{12} = \nu_g a_N \Gamma_r\Gamma_z\{(1 - \varepsilon_s S_0/N_{p0})S_0/N_{p0} + \varepsilon_s \ln(N_{p0}/N_t)(S_0/N_{p0})^2\} + 2\beta B_{sp}N_{p0} \tag{B7}$$

$$1/T_{21} = \nu_g a_N \Gamma_p\Gamma_z \ln(N_{p0}/N_t)(1 - 2\varepsilon_s S_0/N_{p0}) \tag{B8}$$

$$1/T_{22} = \nu_g a_N \Gamma_p\Gamma_z\{(1 - \varepsilon_p S_0/N_{p0})S_0/N_{p0} + \varepsilon_p \ln(N_{p0}/N_t)(S_0/N_{p0})^2\} - 1/\tau_{21}'. \tag{B9}$$

The resonance frequency ω_n $(= \Omega)$ of the device satisfies (B5) and is given by

$$\omega_n^2 \approx 1/T_{12}T_{21} + 1/T_{11}T_{22} + 1/\tau_{12}(1/T_{11} + T_{22} - 1/\tau_{21}) \tag{B10}$$

where we have assumed $\tau_{12} \approx \tau_{12}'$. As we can see from (B10), ω_n is inversely proportional to τ_{12} provided that $1/T_{11} + 1/T_{22} > 1/\tau_{21}$, and this is confirmed by Fig. 7(b). In (B10), the resonance frequency can be maximized by carefully designing the dimension of active quantum wells and spacer layers such that $\tau_{12} \ll \tau_{21}$ and $1/T_{11} + 1/T_{22} \gg 1/\tau_{21}$ (i.e., $\tau_{12} < 10$ ps and $\tau_{21} > 400$ ps).

If we omit the terms representing the carrier transport effects (i.e., τ_{21} and τ_{21}) and the spontaneous emission rate, (B10) can be rewritten as

$$\omega_n^2 \approx (\nu_g a_N \Gamma_z)^2 \Gamma_r\Gamma_p \ln\left(\frac{N_{p0}}{N_t}\right)\left(\frac{S_0}{N_{p0}}\right)\left\{1 - \varepsilon_s\frac{S_0}{N_{p0}}\left(3 - \ln\left(\frac{N_{p0}}{N_t}\right)\right) + \frac{S_0}{N_{p0}}\right\}. \tag{B11}$$

Furthermore, we can also ignore the influence of spatial hole burning, set $\Gamma_p = \Gamma_1 + D\chi_1\tau_c\Gamma_2 \approx \Gamma_1$, and assume $S_0/N_{p0} \gg 1$ for high-power operation, and (B11) can then be written as

$$\omega_n^2 \approx \Gamma_r\Gamma_1(\nu_g a_N \Gamma_z)^2 \ln(N_{p0}/N_t)(S_0/N_{p0})^2. \tag{B12}$$

REFERENCES

[1] T. G. Dziura, Y. J. Yang, R. Fernandez, T. Bardin, and S. C. Wang, "High speed modulation characteristics of Helium-implanted Zinc-diffused vertical cavity surface emittin lasers," *IEEE Photon. Technol. Lett.*, vol. 5, pp. 1270–1292, 1993.

[2] J. W. Scott, B. J. Thibeault, C. J. Mahon, L. A. Coldren, and F. H. Peters, "High modulation efficiency of intracavity vertical cavity lasers," *Appl. Phys. Lett.*, vol. 65, no. 120, pp. 1483–1485, 1994.

[3] J. W. Scott, R. S. Geels, S. W. Corzine, and L. A. Coldren, "Modeling temperature effects and spatial hole burning to optimize vertical cavity surface emitting laser performance," *IEEE J. Quantum Electron.*, vol. 29, pp. 1295–1308, 1993.

[4] R. Michalzik and K. J. Ebeling, "Modeling and design of proton-implanted ultralow-threshold vertical-cavity laser diodes," *IEEE J. Quantum Electron.*, vol. 29, pp. 1963–1974, 1993.

[5] R. S. Tucker and D. J. Pope, "Cirucit modeling of the effect of diffusion on damping in a narrow-stripe semiconductor laser," *IEEE J. Quantum Electron.*, vol QE-19, pp. 1179–1183, 1983.

[6] N. Bewtra, D. A. Suda, G. L. Tan, F. Chatenoud, and J. M. Xu, "Modeling of quantum well lasers with electro-opto-thermal interaction," *IEEE J. Select. Topics Quantum Electron.*, vol 1, pp. 331–340, 1995.

[7] T. A. DeTemple and C. M. Herzinger, "On the semiconductor laser logarithmic gain-current density relation," *IEEE J. Quantum Electron.*, vol 29, pp. 1246–1252, 1993.

[8] S. F. Yu, "Dynamic behavior of vertical cavity surface emitting lasers," *IEEE J. Quantum Electron.*, vol. 32, pp. 1168–1179, 1996.

[9] N. K. Dutta, J. Lopata, D. L. Sivco, and A. Y. Cho, "Temperature dependence of threshold of strained quantum well lasers," *Appl. Phys. Lett.*, vol. 58, no. 11, pp. 1125–1127, 1991.

[10] R. S. Zory, Ed., *Quantum Well Lasers*. New York: Academic, 1993, ch. 1.

[11] Y. G. Zhao and J. G. McInerney, "Transient temperature response of vertical cavity surface emitting semiconductor lasers," *IEEE J. Quantum Electron.*, vol 31, pp. 1668–1673, 1995.
[12] M. Ogura and H. C. Hsieh, "Effect of surface recombination velocity on the threshold current and differential quantum efficiency of the surface emitting laser diode," *IEEE J. Quantum Electron.*, vol 32, pp. 597–606, 1996.
[13] G. Morthier, F. Libbrecht, K. David, P. Vankwikelberge, and R. G. Baets, "Theoretical investigation of the second order harmonic distortion in the AM response of 1.55 μm F-P and DFB lasers," *IEEE J. Quantum Electron.*, vol 27, pp. 1990–2002, 1991.

S. F. Yu, for photograph and biography, see p. 1179 of the July issue of this JOURNAL.

W. N. Wong, photograph and biography not available at the time of publication.

P. Shum was born in the northern part of China in 1968. He received the B.Eng. degree in electronic and electrical engineering and the Ph.D. degree from the University of Birmingham in 1991 and 1995, respectively.

After graduation, he worked at Birmingham University as an Honorary Research Fellow. He is currently doing his postdoctoral research at Hong Kong University. His research interests are concerned with the formation and propagation of solitons in both optical and electrical devices, nonlinear modeling, and analysis of vertical-cavity surface-emitting lasers.

E. Herbert Li (S'87–M'88–SM'95), for photograph and biography, see p. 1415 of the August issue of this JOURNAL.